

# Information Entropy-Based Framework for Quantifying Tortuosity in Meibomian Gland Uneven Atrophy

Kesheng Wang, Xiaoyu Chen, Chunlei He, Fenfen Li, Xinxin Yu, Dexing Kong, Shoujun Huang, Qi Dai

**Abstract**—In the medical image analysis field, precise quantification of curve tortuosity plays a critical role in the auxiliary diagnosis and pathological assessment of various diseases. In this study, we propose a novel framework for tortuosity quantification and demonstrate its effectiveness through the evaluation of meibomian gland atrophy uniformity, serving as a representative application scenario.

We introduce an information entropy-based tortuosity quantification framework that integrates probability modeling with entropy theory and incorporates domain transformation of curve data. Unlike traditional methods such as curvature or arc-chord ratio, this approach evaluates the tortuosity of a target curve by comparing it to a designated reference curve. Consequently, it is more suitable for tortuosity assessment tasks in medical data where biologically plausible reference curves are available, providing a more robust and objective evaluation metric without relying on idealized straight-line comparisons.

First, we conducted numerical simulation experiments to preliminarily assess the stability and validity of the method. Subsequently, the framework was applied to quantify the spatial uniformity of meibomian gland atrophy and to analyze the difference in this uniformity between *Demodex*-negative and *Demodex*-positive patient groups. The results demonstrated a significant difference in tortuosity-based uniformity between the two groups, with an area under the curve of 0.8768, sensitivity of 0.75, and specificity of 0.93. These findings highlight the clinical utility of the proposed framework in curve tortuosity analysis and its potential as a generalizable tool for quantitative morphological evaluation in medical diagnostics.

**Index Terms**— *Demodex* infestation, Information entropy, Meibomian gland atrophy, Morphological assessment, Tortuosity.

This research was funded by the grants from Zhejiang Normal University (Grant Nos. YS304222929, YS304222977, PTK12923007, PTK12923012), and the National Natural Science Foundation of China (Grant Nos. 12090020 and 12090025), and the State Administration of traditional Chinese medicine Science and Technology Department-Zhejiang Provincial Administration of Traditional Chinese Medicine Co-construction Science and Technology Plan (Grant No. GZY-ZJ-KJ-23086). Corresponding authors: Shoujun Huang and Qi Dai.

Kesheng Wang, Chunlei He, Dexing Kong, Shoujun Huang and Qi Dai are with College of Mathematical Medicine, Zhejiang Normal University, Jinhua 321004, China, (e-mails: 2583510768@zjnu.edu.cn; chunlei@zjnu.edu.cn; dkong@zjnu.edu.cn; sjhuang@zjnu.edu.cn; dq@mail.eye.ac.cn).

Xiaoyu Chen, Fenfen Li, Xinxin Yu and Qi Dai are with National Clinical Research Center for Ocular Diseases, Eye Hospital, Wenzhou Medical University, Wenzhou 325027, China, (e-mails: xiaoyuchenny@wmu.edu.cn; lfenfen@eye.ac.cn; 13588775204@eye.ac.cn; dq@mail.eye.ac.cn).

## I. INTRODUCTION

THE tortuosity of anatomical curves is crucial in clinical medical image analysis and has been widely applied in the auxiliary diagnosis and pathological evaluation of various diseases. For example, the tortuosity of retinal blood vessels in neonates serves as a crucial indicator for diagnosing retinopathy of prematurity, providing insights into the degree of abnormal neovascularization and disease progression [1]. Similarly, corneal nerve tortuosity plays an important role in the assessment of several neuropathic conditions, such as diabetic neuropathy and autoimmune disorders, as it reflects the status of nerve fiber damage and regeneration [2]–[5]. In addition, for meibomian gland dysfunction (MGD), the tortuosity of the glandular boundary curves has been proposed as an indirect marker for evaluating the spatial uniformity of gland atrophy, thereby offering a quantitative basis for the early identification and intervention of related ocular surface diseases [6]–[13].

Previous studies have demonstrated a strong association between ocular *Demodex* infestation and MGD, with the presence of mites shown to disrupt the normal morphology and function of the meibomian glands [7], [14], [15]. The pathogenic mechanisms of *Demodex* are multifactorial, including mechanical obstruction of glandular orifices, release of toxic metabolic byproducts, induction of inflammatory and immune responses, and synergistic effects with bacterial colonization—all of which contribute to ocular surface damage. Clinically, *Demodex* infestation has been observed to induce characteristic focal or irregular atrophy of the meibomian glands [6]–[13]. However, despite these observations, the underlying mechanisms and structural manifestations of this nonuniform atrophy remain poorly understood, and there is currently no standardized method for its quantitative assessment. Therefore, developing objective and robust approaches to characterize the spatial distribution of glandular atrophy—particularly in relation to tortuosity-derived measures of structural uniformity—may offer valuable insights for the early detection of *Demodex* infestation, facilitate more refined clinical evaluation, and support future investigations into its pathological mechanisms.

## II. RELATED WORK

Currently, in vivo confocal microscopy (IVCM) is the clinical gold standard for diagnosing *Demodex* blepharitis.

However, this method requires a high level of patient cooperation and involves considerable time and cost, limiting its widespread use. The evaluation of meibomian gland atrophy uniformity associated with *Demodex* blepharitis still primarily relies on subjective expert judgment, with a lack of effective and objective quantitative approaches [16], [17], and related research remains limited [18], [19]. Cross-disciplinary investigations have revealed that curve tortuosity assessment has various definitions and computational methods [20]–[22]. Representative metrics include chord-to-arc ratio, curvature, least squares linear regression, and total variation, along with various extensions and improvements built upon these foundational techniques [20], [22]–[33]. These methods have been successfully applied in the analysis of medical images involving extracranial internal carotid arteries [29], coronary arteries [31], temporal arteries and veins [33], as well as retinal vasculature [23], [25], [30].

However, these methods generally rely on comparing the target curve to an ideal straight line to quantify the degree of deviation, which presents inherent limitations in real-world clinical imaging scenarios. For instance, for meibomian glands, the boundary curves of healthy glands naturally exhibit a certain degree of physiological tortuosity. Therefore, using a straight line as the reference may fail to accurately reflect structural alterations. In contrast, employing a nonlinear reference is often more consistent with physiological reality. As a result, traditional approaches may be limited in their ability to distinguish pathological tortuosity from normal anatomical variation.

To address this, we propose a novel information entropy-based framework (IEBF) for evaluating curve tortuosity. This method structurally compares the target curve under evaluation with a predefined standard curve and quantifies the degree of disorder in their difference space using information entropy, thereby assessing the tortuosity of the target curve. Furthermore, *Demodex* blepharitis is used as a clinical validation scenario, where the tortuosity of the meibomian gland boundary curve serves as an indicator of meibomian gland atrophy uniformity. Additionally, the effectiveness of the proposed method in distinguishing *Demodex* infection is evaluated. Experimental results demonstrate that the framework can effectively quantify the uniformity of meibomian gland atrophy and accurately differentiate between infected and non-infected cases. Compared to existing traditional methods, it shows significant advantages in clinical discriminative performance and exhibits promising potential for clinical application.

### III. MATERIALS

#### A. Data and Equipment

This retrospective study was conducted at the Hangzhou campus of Wenzhou Medical University Eye Hospital from December 2023 to September 2024. It focused on patients who visited the hospital due to eye discomfort and underwent IVCN. Patients with negative results for *Demodex* on this microscopy were included. Meanwhile, patients with *Demodex* blepharitis, confirmed by positive mite infection on the same microscopy during the same period, were collected as controls.

According to the Chinese expert consensus on diagnosis and treatment of *Demodex* blepharitis, the diagnostic criteria for *Demodex* blepharitis include: (1) chronic or subacute bilateral ocular symptoms such as redness, itching, foreign body sensation, or recurrent, refractory chalazion; (2) abnormal eyelashes with sebaceous sleeve-like secretions at the eyelash roots (a diagnostic indicator), possibly accompanied by eyelid margin hyperemia and thickening; and (3) positive *Demodex* examination. Patients' meibography images were captured using the Keratograph 5M (K5M; Oculus, Wetzlar, Germany). The images of the right upper eyelid were included for analysis.

All images were acquired at a resolution of  $1360 \times 1024$  and saved in bmp format. After excluding images with poor quality or insufficient clarity for analysis, 35 patients were included in the *Demodex*-negative group and 70 in the *Demodex*-positive group.

The study was conducted in accordance with the Declaration of Helsinki (as revised in 2013). This study was approved by the Institutional Review Board (IRB) of the Eye Hospital, Wenzhou Medical University (IRB approval No. H2023-045-K-42) and the requirement for individual consent for this retrospective analysis was waived due to the retrospective nature.

The parameter settings of the meibomian gland segmentation model, as well as the hardware configuration used for its training and testing, followed those reported by Zhang et al. [34]. The development of the curvature algorithm and related experiments were conducted on hardware equipped with a 13th Gen Intel(R) Core(TM) i7-13700KF processor operating at 3.40 GHz. The software environment consisted of Windows 11 as the operating system, PyCharm Community Edition 2024.3.1 (JetBrains, Prague, Czech Republic) as the development platform, and Python 3.12.8 (Python Software Foundation, Wilmington, USA) as the programming language.

#### B. STATISTICAL ANALYSIS

All statistical analyses in this study were performed in the Python environment (version 3.12.8). Key libraries used include numpy and pandas for data processing, scipy.stats for statistical testing, matplotlib and seaborn for visualization, and sklearn.metrics for performance evaluation and receiver operating characteristic (ROC) analysis.

We calculated and performed descriptive statistical analysis on the tortuosity data of the two groups. Descriptive statistics were presented as mean  $\pm$  standard deviation (SD) or median (interquartilerange, IQR). The normality of the data distribution was assessed using the Shapiro-Wilk test. Based on the results of the normality test, appropriate methods were selected for intergroup comparison: an independent samples t-test was used if the data were approximately normally distributed; otherwise, the nonparametric Mann-Whitney U test was applied.

The distribution characteristics of the tortuosity data from the two groups were visually compared using boxplots. Additionally, to evaluate the effectiveness of the proposed framework in discriminating *Demodex* blepharitis, ROC curves were plotted. The overall classification performance was quantified

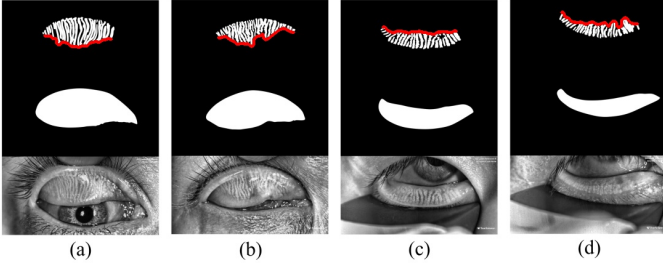


Fig. 1: Meibomian gland segmentation and boundary extraction. (a, c): *Demodex*-negative group; (b, d): *Demodex*-positive group. Each panel shows (top to bottom): boundary map (red curve), tarsal region, and original image.

by calculating the area under the curve (AUC), and the optimal classification threshold was determined using the Youden index to achieve the best balance between sensitivity and specificity. This analysis confirmed that the proposed entropy-based metric possesses strong discriminative ability for identifying *Demodex* infection status and holds promising clinical application value.

#### IV. METHODS

##### A. Boundary Extraction and Refinement

This study employed the meibomian gland segmentation model developed by Zhang *et al.* [34] to segment meibomian glands from meibography images. Based on the segmentation results, an effective boundary extraction method was proposed.

Panels (a) and (c) of Fig 1 show relatively uniform gland distribution in the *Demodex*-negative group, whereas panels (b) and (d) represent the *Demodex*-positive group, displaying characteristic uneven atrophy. Each image consists, from top to bottom, of the refined gland segmentation map, tarsal plate region map, and original image. The red curves indicate the extracted and optimized boundaries of the meibomian glands. The detailed processing steps are as follows:

First, the image is smoothed through Gaussian filtering using the following two-dimensional Gaussian kernel:

$$G(i, j) = \frac{1}{2\pi\sigma^2} \cdot e^{-\frac{i^2+j^2}{2\sigma^2}}. \quad (1)$$

The image is convolved with the Gaussian kernel to obtain the blurred image

$$I'(x, y) = \sum_{i=-k}^k \sum_{j=-k}^k G(i, j) \cdot I(x+i, y+j), \quad (2)$$

where  $i$  and  $j$  represent the coordinate offsets relative to the center of the Gaussian kernel;  $\sigma$  is the SD of the Gaussian kernel,  $G(i, j)$  denotes the weight of the Gaussian kernel at position  $(i, j)$ ;  $I(i, j)$  and  $I'(i, j)$  represent the grayscale values of the input and output (blurred) images at the corresponding positions, respectively.  $k$  is the radius of the Gaussian kernel. In this study, the parameters were set as  $\alpha = 0$  and  $k = 51$ . These parameters were determined based on empirical results that yielded optimal performance.

The boundary information of the meibomian gland region is initially extracted from the output image. Subsequently,

an active contour model is employed to further optimize the curve's position, where the energy function is defined by

$$E = \int (E_{internal}(s) + E_{external}(s)) ds, \quad (3)$$

in which

$$E_{internal}(s) = \alpha \left\| \frac{dv(s)}{ds} \right\|^2 + \beta \left\| \frac{d^2v(s)}{ds^2} \right\|^2, \quad (4)$$

$$E_{external}(s) = -|\nabla I(v(s))|. \quad (5)$$

Note that  $E_{internal}$  represents the smoothness and continuity of the curve, typically related to its bending degree;  $E_{external}$  reflects the relationship between the curve and the image edges, encouraging the curve to move toward the true boundary of the meibomian gland region. To minimize the energy function, we need to compute the gradient of the total energy with respect to each point on the curve. The gradient indicates the direction and rate of change of the energy function at that point, guiding the movement of the curve. For each point  $X_i = (s_i, v(s_i))$ , the gradient can be expressed as

$$\nabla E(X_i) = \nabla E_{internal}(X_i) + \nabla E_{external}(X_i). \quad (6)$$

Each point on the curve is updated using the gradient descent method. By moving in the direction opposite to the gradient, the energy gradually decreases, and the curve evolves toward the position of minimum energy. The updated formula is given by

$$X_{i,j+1} = X_{i,j} - \mu \nabla E(X_i), \quad (7)$$

where  $X_i$  denotes the coordinate of the  $i$ -th point on the curve at the  $t$  iteration,  $\mu$  is the step size controlling the movement speed of the curve points during each iteration, and  $\nabla E(X_i)$  is the gradient of the energy function at point  $X_i$ . Through this updated formula, the curve gradually evolves toward the minimum energy state until convergence is reached, yielding the optimized boundary curve. In this study, the parameters were set as  $\alpha = 0.1$ ,  $\beta = 1.0$  and  $\mu = 0.1$ . These parameters were also determined based on empirical results that yielded optimal performance.

In this study, the extremal points of the optimized boundary curve are used to truncate the curve, retaining only the segment between the two extreme points. This process effectively adjusts the extracted curve to better conform to the true boundary of the meibomian gland region while ensuring the smoothness and continuity of the curve. This approach significantly improves the accuracy of boundary extraction.

##### B. Calculation of the Curve Tortuosity

This study proposes that the evaluation of curve tortuosity requires a reference standard curve as a baseline. The standard curve is defined as an ideally unbent curve under a specific task, whereas the curve to be evaluated is referred to as the target curve. To quantify the difference between the target and baseline curves, we present an IEBF for tortuosity calculation.

Information entropy is a metric used to assess the uncertainty or disorder within a system. For a set of discrete data

points, higher entropy indicates more greater variability and uncertainty among the points, whereas lower entropy suggests more uniformity. Mathematically, information entropy is typically defined by

$$H(X) = - \sum_{i=1}^n p(x_i) \cdot \log(p(x_i)), \quad (8)$$

where  $H(X)$  denotes the information entropy of random variable  $X$ ,  $x_i$  represents the  $i$ -th possible value of  $X$ ,  $p(x_i)$  denotes the probability that  $X$  takes the value  $x_i$ , and  $n$  is the total number of possible values that  $X$  can take.

When calculating the curve tortuosity, we evaluate the characteristics of distribution of point-wise distance differences between the target and baseline curves, and measure the tortuosity by quantifying the magnitude of disorder of these differences. The specific procedure is as follows.

### 1) Construct the Point-to-Point Distance Difference Vector:

Assume there are two discrete curves located on the same plane. The first curve is the standard curve, composed of  $n$  coordinate points, and it is denoted by  $y = f_1(x)$ . The second curve is the target curve, also composed of  $n$  coordinate points, and is denoted as  $y = f_2(x)$ . The domain for both curves is assumed to be the same (i.e.,  $[a, b]$ ). Let  $s$  be a constant representing the sampling interval. Introduce the following notations:

$$\delta_k = f_1(a + ks) - f_2(a + ks), \quad (9)$$

$$\alpha = \|\delta_{l+1}\| - \|\delta_l\|, \quad (10)$$

$$\beta = \|\delta_{l-1}\| - \|\delta_l\|, \quad (11)$$

where  $l \in \mathbb{Z}^+$ ,  $l \leq \lfloor \frac{b}{s} \rfloor = q$ . The distance difference vector is then

$$d_l = \frac{1}{2} \|\alpha\| + \frac{1}{2} \|\beta\|. \quad (12)$$

We collect all the distance differences in the form of a vector

$$D = (d_1, d_2, \dots, d_q). \quad (13)$$

The schematic diagram of this process is shown in Fig 2.

2) *Construction of the Probability Vector:* The standard Gaussian probability density function is given by

$$f(d) = \frac{1}{\sqrt{2\pi\sigma^2}} e^{-\frac{(d-\mu)^2}{2\sigma^2}}, \quad (14)$$

where we take  $\mu = 0$ ,  $\sigma = 1$ . The corresponding probability function is expressed as

$$g(x) = \int_{-\infty}^x f(t) dt. \quad (15)$$

Using the probability function, the distance vector can be transformed into a probability vector

$$P = (g(d_1), g(d_2), \dots, g(d_q)). \quad (16)$$

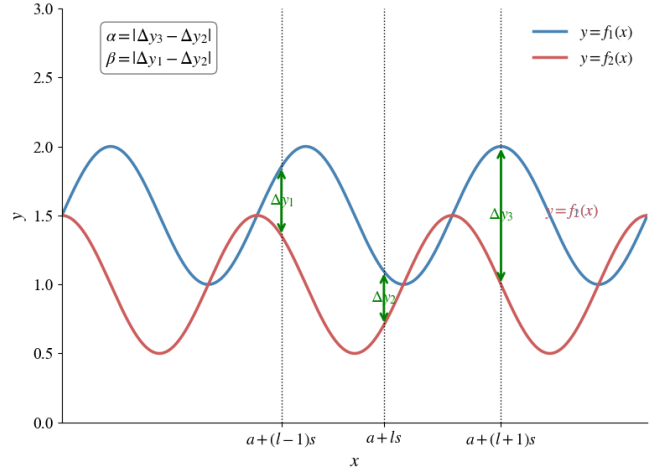


Fig. 2: Schematic diagram of the construction of the point-to-point distance difference vector.

3) *Construction of the Tortuosity Mapping:* Based on the above discussion, we introduce the concept of total tortuosity, which is computed using the following formula

$$e(P) = \left( -\frac{1}{q} \sum_{p=1}^q (1 - 2g(d_p)) \cdot \log(2g(d_p)) \right)^{\frac{1}{2}}. \quad (17)$$

This expression can be regarded as an entropy-based approximation function incorporating both distance and probability. Here,  $e(P)$  denotes the entropy value, and  $g(d_p)$  is a function applied to the distance difference  $d_p$ . Because the range of value  $g(d_p)$  is  $(0, \frac{1}{2})$ , it is scaled by a factor of 2 to extend the range to  $(0, 1)$ . As  $d_p$  increases,  $g(d_p)$  decreases; when  $d_p = 0$ , we have  $g(d_p) = \frac{1}{2}$ . Therefore, the term  $p \log p$  in the original information entropy is reformulated as  $(1 - p) \log p$ , leading to Eq. (17)

### C. Tortuosity Correction

Generally, the real acquired data contains various types of noise, which could affect the tortuosity values. Therefore, the original data is transformed into frequency spaces by using Fourier transform to extract either low-frequency or high-frequency components. The extracted components are then transformed back to the spatial domain via inverse Fourier transform, and tortuosity calculation can be performed. This process allows to focus specifically on either the low- or high-frequency information of the curve.

1) *Fourier Transform:* Given a one-dimensional time-domain signal, its Fourier transform is defined as

$$F(\omega) = \frac{1}{2\pi} \int_{-\infty}^{+\infty} f(x) e^{-i\omega x} dx, \quad (18)$$

where  $f(x)$  is the time-domain signal, representing a function over time (or space).  $F(\omega)$  is the frequency-domain signal, describing the distribution of the signal over different frequencies.  $\omega$  is the angular frequency, which is related to frequency  $\xi$  by  $\omega = 2\pi\xi$ , with units of radians per second.  $i$  is the imaginary unit.

2) **Frequency Band Extraction:** Low-frequency components ( $F_{low}(\omega)$ ) typically represent the overall trend or slowly varying part of the signal, whereas high-frequency components ( $F_{high}(\omega)$ ) contain rapidly changing details or noise. By defining a low-frequency cutoff point ( $\omega_L$ ), the low-frequency portion of the signal can be extracted; similarly, a high-frequency cutoff point ( $\omega_H$ ) is used to isolate the high-frequency part. That is

$$F_{low}(\omega) = \begin{cases} F(\omega), & \text{if } |\omega| \leq \omega_L \\ 0, & \text{if } |\omega| > \omega_L \end{cases}, \quad (19)$$

$$F_{high}(\omega) = \begin{cases} F(\omega), & \text{if } |\omega| \geq \omega_H \\ 0, & \text{if } |\omega| < \omega_H \end{cases}. \quad (20)$$

3) **Inverse Fourier Transform:** The extracted frequency bands (low- or high-frequency components) are transformed back to the original domain through the inverse Fourier transform. This allows us to observe the contribution of each frequency band within the original signal. Given a frequency-domain signal, the inverse Fourier transform converts it back to the time-domain signal. The formula for the inverse Fourier transform is

$$f(x) = \frac{1}{2\pi} \int_{-\infty}^{+\infty} F(\omega) e^{i\omega x} d\omega. \quad (21)$$

By integrating the analysis of both low- and high-frequency information, a comprehensive evaluation of tortuosity at global and local scales can be achieved. This analytical approach not only enhances the accuracy of tortuosity calculation, but also better captures the complex characteristics of the data, thereby providing more reliable support for research and applications in related fields.

## V. EXPERIMENTS AND RESULTS ANALYSIS

### A. Numerical Experiment on Tortuosity Quantification

Owing to the difficulty of obtaining clinical data and the complexity and time-consuming nature of the curve extraction process, this study first conducts numerical experiments to preliminarily validate the effectiveness and stability of the proposed method. After validation, the method is further applied to real clinical data for additional verification.

First, a sine curve was generated as the reference curve. Then, Gaussian random noise with a mean ( $\mu$ ) of 0 and SDs ( $\sigma$ ) ranging from 0.0 to 0.9 at 10 different levels was added to the curve. For each noise level, 5000 random target curves were generated for experimental validation. The average computation time for curvature evaluation per curve was approximately 0.0356 s. Figure 3 illustrates the selected standard curves (in blue) and corresponding target curves (in red) at four different noise levels. Figure 4a shows the low-frequency components of the target curves at various noise levels, whereas Fig. 4b presents the corresponding high-frequency components. Specifically, when the noise level is 0.0, the curves represent the low- or high-frequency characteristics of the standard curve. The average tortuosity of all target curves was calculated using the IEBF method, and the trend across different levels of Gaussian noise was plotted, as shown in Fig. 5a. The tortuosity variations of the low- and high-frequency components of the target curves under different noise intensities are shown in Figs. 5b and 5c, respectively.

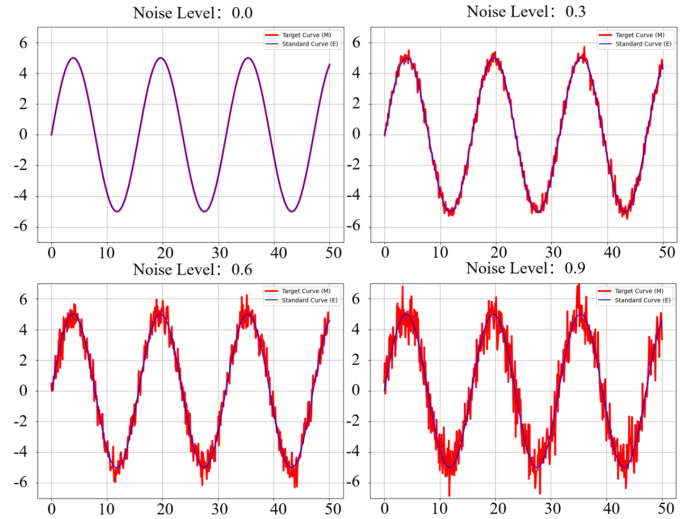


Fig. 3: Comparison of target curves and standard curve under different levels of gaussian noise.

As shown in Fig. 5a, the tortuosity of the target curve increases monotonically with the noise level, indicating that the proposed method can effectively quantify the tortuosity of target data relative to the standard curve. When Gaussian noise is added at the highest level (Noise Level = 0.9), the tortuosity of the target curve reaches 12.43. Figures. 5b and 5c show that the tortuosity calculated from both low- and high-frequency components increases gradually with noise level. Because Gaussian noise has minimal impact on the low-frequency components, the maximum tortuosity calculated from the low-frequency information is only 0.53. This method not only effectively quantifies the influence of Gaussian noise on curve tortuosity, but also leverages Fourier transform to filter out high-frequency noise interference, thereby enhancing the robustness of structural analysis.

### B. Experiment on Meibomian Gland Atrophy Uniformity

In this study, 105 subjects, comprising 35 patients in the Demodex-negative group and 70 in the Demodex-positive group, 105 subjects were included, with ages ranging from 26 to 45 years. The average computation time for the atrophy uniformity index per image was approximately 0.6267 s. The Mann-Whitney U test was used to analyze the differences in the gland atrophy uniformity indices between the two groups. The results indicated a statistically significant difference in uniformity indices between the negative and positive groups ( $p < 0.05$ ). The basic demographic information, descriptive statistics, and  $p$ -values from the Mann-Whitney U test are summarized in Table I.

This study employed box plots and ROC curves to visualize the differences in key metrics between the negative and positive groups. As shown in Fig. 6, the box plots clearly illustrate the distributional differences between the two groups across the three methods. Furthermore, Fig. 7 presents the ROC curves of the uniformity indices derived from each method. The corresponding AUC, sensitivity, specificity, and optimal classification thresholds are summarized in Table II. The

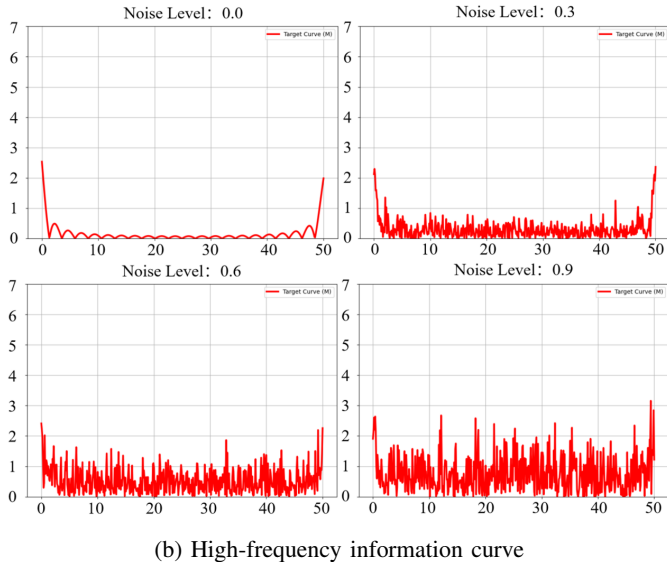
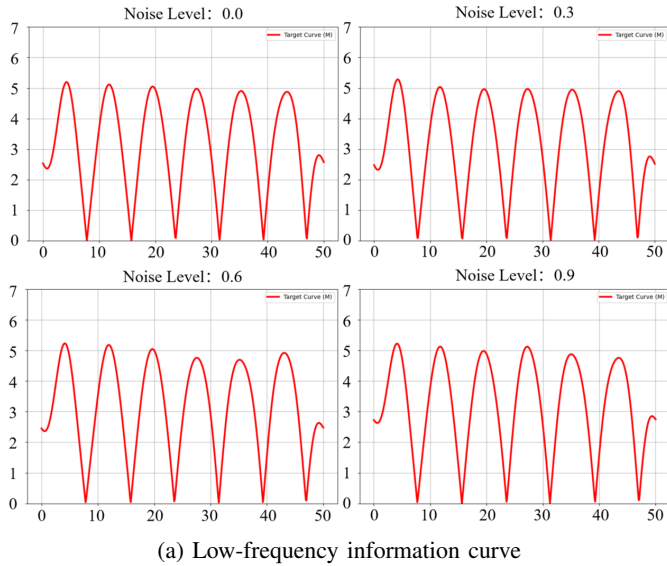


Fig. 4: Low- and high-frequency components of the target curves under varying levels of gaussian noise.

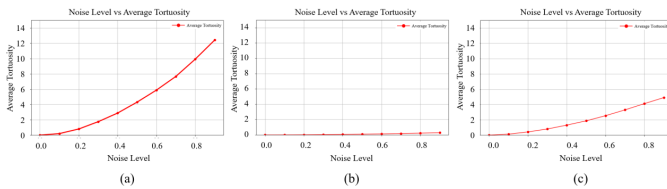


Fig. 5: Tortuosity variation curves of the target curves and their low- and high-frequency components under different levels of gaussian noise. (a) Original target curve (b) Low-frequency information curve (c) High-frequency information curve

results demonstrate that IEBF achieved the best performance in distinguishing between the two groups, with an AUC, sensitivity, and specificity of 0.858, 0.786, and 0.857, respectively, significantly outperforming the other methods and exhibiting superior discriminative capability.

TABLE I: Comparison of Clinical and Quantitative Indicators Between *Demodex* Positive and Negative Groups

	<i>Demodex</i> Negative	<i>Demodex</i> Positive	p
Sex	M=11(31.4%) F=24(68.6%)	M=19(27.1%) F=51(72.9%)	0.647
Age (Years (Mean $\pm$ Std))	35.37 $\pm$ 9.30	36.64 $\pm$ 8.20	0.289
IEBF (Our Method) (Median (IQR))	829.27 (645.51-1094.64)	1916.96 (1298.12-2790.92)	$\leq$ 0.001
Chord-to-Arc Ratio (Median (IQR))	1.52(1.39-1.66)	1.89(1.74-2.21)	$\leq$ 0.001
Total Variation (Median (IQR))	1259.74 (1095.39-1391.53)	1447.21 (1165.76-1667.55)	0.009

M indicates the number and percentage of male participants, and F indicates those of female participants. 'IEBF', 'Chord-to-Arc Ratio', and 'Total Variation' represent the median and interquartile range (IQR) of tortuosity values calculated using the corresponding methods.

TABLE II: Performance Comparison of Different Methods Across Various Metrics

	AUC(95%CI)	Sensitivity	Specificity
IEBF (Our Method)	0.858(0.782-0.921)	0.786	0.857
Chord-to-Arc Ratio	0.811(0.705-0.899)	0.743	0.829
Total Variation	0.656(0.548-0.760)	0.514	0.829

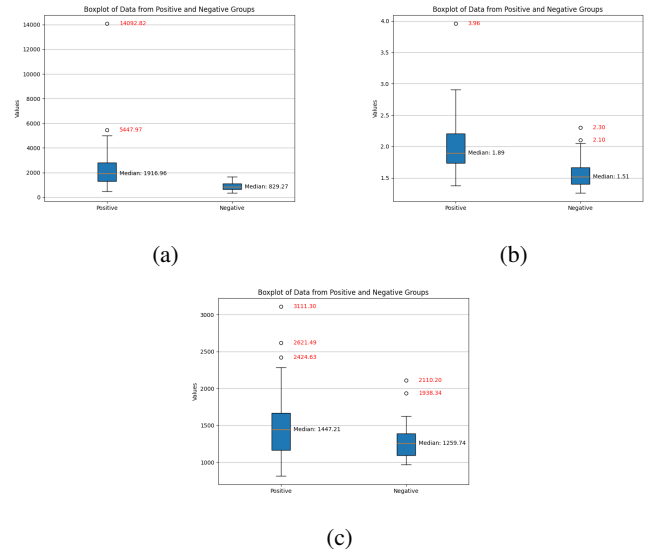


Fig. 6: Box plots of tortuosity results for the normal control and abnormal groups. (a)IEBF (our method), (b) chord-to-arc ratio method, (c)total variation divided by gland density method.

## VI. DISCUSSION

This study proposes a novel tortuosity evaluation metric based on information entropy, which was validated and applied through numerical experiments and a clinical case study of *Demodex* blepharitis. Currently, the diagnosis of *Demodex* blepharitis primarily relies on clinical signs such as lid margin hyperemia, scaling, cylindrical dandruff, eyelash abnormalities, and meibomian gland atrophy; however, these manifestations lack sufficient specificity [35]. The current

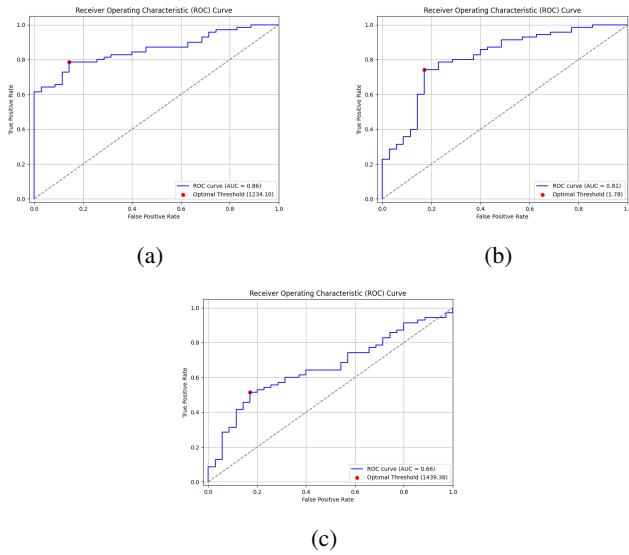


Fig. 7: ROC curve of tortuosity distinguishing the normal control group from the abnormal group. (a)Our method, (b) chord-to-arc ratio method, and (c)total variation divided by gland density method.

gold standard for diagnosing *Demodex* infection includes microscopic examination of epilated eyelashes and confocal microscopy observation of the eyelash roots and eyelid margin. Particularly, confocal microscopy offers non-invasive, high-resolution imaging to detect *Demodex* mites and associated tissue responses [10], [36]. However, this technique is operationally complex, requires specialized equipment and experienced clinicians, and entails lengthy examination times and high costs, limiting its widespread adoption in routine ophthalmic practice. Consequently, clinical diagnosis often depends on subjective assessments, highlighting the need for a more convenient, objective, and cost-effective quantitative method for structural alteration assessment.

Previous studies have suggested that uneven atrophy of the meibomian glands may represent a structural hallmark of *Demodex* infestation, which can be characterized by the curvature of the glandular boundary contour. This feature may help differentiate *Demodex*-related dysfunction from other types of meibomian gland abnormalities. However, no standardized quantitative criteria have been established to incorporate this characteristic into clinical diagnostic workflows, thereby limiting its potential application in practice [18], [37].

To accurately quantify the structural complexity of curves, various tortuosity evaluation methods have been proposed in related studies across multiple disciplines, including ophthalmology, vascular surgery, and neurosurgery. The chord-to-arc ratio method [19], [29], [31], [38], widely favored for computational simplicity, measures overall tortuosity as the ratio of curve length to chord length; however, it fails to capture local detail and multi-scale structural variations of boundary curves. Additionally, it is sensitive to image resolution and noise, which impairs clinical applicability. The total variation method [18] quantifies overall curve morphology by assessing gradient fluctuations but similarly exhibits noise sensitivity.

Curvature-based methods [20]–[27], [29], [30] provide precise local bending characterization; however, they rely heavily on second-order derivatives, rendering them vulnerable to noise-induced instability and limiting their representation of global morphology. In anatomical structures exhibiting natural physiological tortuosity (e.g., meibomian glands, blood vessels, nerves), tortuosity metrics often generate excessive local extrema, complicating differentiation between physiological and pathological variations. Moreover, these methods generally reference ideal straight lines, which inadequately reflect the nonlinear structural features prevalent in biological tissues, often misclassifying normal tortuosity as pathological.

To address these challenges, we introduce an information entropy-based curve tortuosity quantification framework. This approach leverages Fourier transform-based frequency domain decomposition to separate low- and high-frequency components of the target curve, effectively suppressing high-frequency noise interference and enhancing robustness and stability in tortuosity estimation. Building on this, the framework employs information entropy coupled with probabilistic modeling to quantify the “disorder” in structural differences between the target and standard curves, thereby providing a comprehensive characterization of tortuosity. Unlike conventional approaches anchored to straight-line references, this framework enables flexible selection of physiologically relevant standard curves, aligning evaluations with actual anatomical morphology and improving discrimination between pathological and physiological tortuosity changes.

Information entropy, a well-established theoretical measure of system uncertainty and complexity, has been extensively applied in biomedical data analysis including image compression, texture recognition, signal processing, and electroencephalography [39]–[42]. Its inherent advantage in capturing structural complexity makes it a natural candidate for curve tortuosity assessment. Incorporating information entropy into tortuosity quantification not only overcomes the dependency on fixed geometric references inherent in traditional methods; however, it also confers enhanced generalizability, sensitivity, and interpretability. This offers a novel quantitative tool for analyzing structural variations in medical imaging, with promising clinical applications.

The proposed framework demonstrated strong performance in numerical simulation experiments. Furthermore, when applied to clinical cases of *Demodex* blepharitis, it achieved promising discriminative results. Specifically, the diagnostic performance for *Demodex* blepharitis infection yielded an AUC of 0.858, with a sensitivity of 0.786 and a specificity of 0.857, providing an accurate and objective quantitative indicator for evaluating the uneven atrophy of Meibomian glands and enhancing diagnostic efficiency. However, during the study, it was observed that the accuracy of Meibomian gland region segmentation had a significant impact on the discriminative power of the proposed index, with segmentation errors contributing to a reduction in overall classification performance.

However, the proposed evaluation framework still has several limitations. First, it relies heavily on the selection of a reference (standard) curve; inappropriate construction of the

standard curve may affect both the accuracy and generalizability of the assessment. Second, while the Fourier transform is effective for separating frequency components, it has inherent limitations when applied to non-stationary signals or abrupt local variations, potentially leading to loss or blurring of critical local details, thereby impacting the fine recognition of complex boundaries. In addition, the computation of information entropy is relatively resource-intensive, which may hinder real-time application in large-scale clinical datasets. Lastly, further validation across diverse clinical settings and datasets is necessary to ensure the robustness and broad applicability of the proposed framework.

In the future, we aim to further improve the proposed framework by optimizing the construction of the standard curve. Specifically, we plan to enable the standard curve to predict subsequent trends based on the historical trajectory of the target curve. By quantifying the degree of disorder between the actual curve and the predicted trend, we will address the challenge of standard curve selection more effectively. In addition, to overcome the high computational complexity of entropy calculation, we will explore algorithmic optimizations and acceleration strategies to enhance processing efficiency, thereby supporting rapid analysis and real-time application in large-scale clinical datasets. Finally, we will the clinical applicability of this framework by integrating multimodal medical imaging data and conducting disease-specific investigations across diverse clinical domains. Through these advancements, the proposed tortuosity evaluation framework holds promise for widespread use in ophthalmology [1], [23], [25], [30], neurosurgery [29], vascular surgery [31], [33], and other clinical disciplines, providing a more reliable quantitative tool for early diagnosis and personalized treatment.

## VII. CONCLUSION

This study proposes a novel curve tortuosity quantification framework that integrates probabilistic modeling and information entropy theory, incorporating frequency-domain transformation of curve data to achieve an objective quantification of structural complexity. Unlike traditional tortuosity or chord-to-arc ratio methods, this approach does not rely on ideal straight lines as references; instead, it quantifies the “disorder” in structural differences by comparing target curves with standard reference curves, thereby providing a more robust and adaptable tortuosity metric. The framework demonstrates strong stability in numerical simulations and has been successfully applied to quantitatively analyze uneven meibomian gland atrophy in patients with *Demodex* blepharitis, exhibiting excellent discriminative capability. This work extends the application of information entropy and probabilistic models in medical curve analysis, offering novel insights and methodologies for quantifying structural changes in clinical imaging, with promising potential for broader adoption.

## REFERENCES

- [1] M. F. Chiang, G. E. Quinn, A. R. Fielder, S. R. Ostmo, R. V. Paul Chan, A. Berrocal *et al.*, “International classification of retinopathy of prematurity, third edition,” *Ophthalmology*, vol. 128, no. 10, pp. e51–e68, 2021.
- [2] A. You, J. K. Kim, I. H. Ryu, and T. K. Yoo, “Application of generative adversarial networks (gan) for ophthalmology image domains: a survey,” *Eye and Vision*, vol. 9, no. 1, p. 6, 2022.
- [3] B. M. Williams, D. Borroni, R. Liu, Y. Zhao, J. Zhang, J. Lim *et al.*, “An artificial intelligence-based deep learning algorithm for the diagnosis of diabetic neuropathy using corneal confocal microscopy: a development and validation study,” *Diabetologia*, vol. 63, no. 2, pp. 419–430, 2020.
- [4] S. Wei, F. Shi, Y. Wang, Y. Chou, and X. Li, “A deep learning model for automated sub-basal corneal nerve segmentation and evaluation using in vivo confocal microscopy,” *Translational Vision Science & Technology*, vol. 9, no. 2, p. 32, 2020.
- [5] A. Cruzat, Y. Qazi, and P. Hamrah, “In vivo confocal microscopy of corneal nerves in health and disease,” *Ocular Surface*, vol. 15, no. 1, pp. 15–47, 2017.
- [6] Y. Y. Gao, M. A. Di Pascuale, W. Li, A. Baradaran-Rafii, A. Elizondo, C. L. Kuo *et al.*, “In vitro and in vivo killing of ocular demodex by tea tree oil,” *British Journal of Ophthalmology*, vol. 89, no. 11, pp. 1468–1473, 2005.
- [7] A. Kheirkhah, V. Casas, W. Li, V. K. Raju, and S. C. Tseng, “Corneal manifestations of ocular demodex infestation,” *American Journal of Ophthalmology*, vol. 143, no. 5, pp. 743–749, 2007.
- [8] S. H. Lee, Y. S. Chun, J. H. Kim, E. S. Kim, and J. C. Kim, “The relationship between demodex and ocular discomfort,” *Investigative Ophthalmology & Visual Science*, vol. 51, no. 6, pp. 2906–2911, 2010.
- [9] S. Cheng, M. Zhang, H. Chen, W. Fan, and Y. Huang, “The correlation between the microstructure of meibomian glands and ocular demodex infestation: A retrospective case-control study in a chinese population,” *Medicine (Baltimore)*, vol. 98, no. 19, 2019.
- [10] M. Randon, H. Liang, M. El Hamdaoui, R. Tahiri, L. Batellier, A. Denoyer *et al.*, “In vivo confocal microscopy as a novel and reliable tool for the diagnosis of demodex eyelid infestation,” *British Journal of Ophthalmology*, vol. 99, no. 3, pp. 336–341, 2015.
- [11] O. Alver, S. A. Kivanc, B. Akova Budak, N. U. Tuzemen, B. Ener, and A. T. Ozmen, “A clinical scoring system for diagnosis of ocular demodicosis,” *Medical Science Monitor*, vol. 23, pp. 5862–5869, 2017.
- [12] X. B. Zhang, Y. H. Ding, and W. He, “The association between demodex infestation and ocular surface manifestations in meibomian gland dysfunction,” *International Journal of Ophthalmology*, vol. 11, no. 4, pp. 589–592, 2018.
- [13] Y. Yan, Q. Yao, Y. Lu, C. Shao, H. Sun, Y. Li *et al.*, “Association between demodex infestation and ocular surface microbiota in patients with demodex blepharitis,” *Frontiers in Medicine*, vol. 7, p. 592759, 2020.
- [14] L. Liang, X. Ding, and S. C. Tseng, “High prevalence of demodex brevis infestation in chalazia,” *American Journal of Ophthalmology*, vol. 157, no. 2, pp. 342–348.e1, 2014.
- [15] Y. Hao, X. Zhang, J. Bao, L. Tian, and Y. Jie, “Demodex folliculorum infestation in meibomian gland dysfunction related dry eye patients,” *Frontiers in Medicine*, vol. 9, p. 833778, 2022.
- [16] R. K. Saha, A. M. M. Chowdhury, K. S. Na, G. D. Hwang, Y. Eom, J. Kim *et al.*, “Automated quantification of meibomian gland dropout in infrared meibography using deep learning,” *Ocular Surface*, vol. 26, pp. 283–294, 2022.
- [17] S. Li, Y. Wang, C. Yu, Q. Li, P. Chang, D. Wang *et al.*, “Unsupervised learning based on meibography enables subtyping of dry eye disease and reveals ocular surface features,” *Investigative Ophthalmology & Visual Science*, vol. 64, no. 13, p. 43, 2023.
- [18] X. Liu, Y. Fu, D. Wang, S. Huang, C. He, X. Yu *et al.*, “Uneven index: A digital biomarker to prompt demodex blepharitis based on deep learning,” *Frontiers in Physiology*, vol. 13, p. 934821, 2022.
- [19] X. Lin, Y. Fu, L. Li, C. Chen, X. Chen, Y. Mao *et al.*, “A novel quantitative index of meibomian gland dysfunction, the meibomian gland tortuosity,” *Translational Vision Science & Technology*, vol. 9, no. 9, p. 34, 2020.
- [20] J. Mao, Y. Luo, L. Liu, J. Lao, Y. Shao, M. Zhang *et al.*, “Automated diagnosis and quantitative analysis of plus disease in retinopathy of prematurity based on deep convolutional neural networks,” *Acta Ophthalmologica*, vol. 98, no. 3, pp. e339–e345, 2020.
- [21] Ö. Smedby, N. Högman, S. Nilsson, U. Erikson, A. G. Olsson, and G. Walldius, “Two-dimensional tortuosity of the superficial femoral artery in early atherosclerosis,” *Journal of Vascular Research*, vol. 30, no. 4, pp. 181–191, 2008.
- [22] W. E. Hart, M. Goldbaum, B. Côté, P. Kube, and M. R. Nelson, “Measurement and classification of retinal vascular tortuosity,” *International Journal of Medical Informatics*, vol. 53, no. 2, pp. 239–252, 1999.
- [23] S. M. Sharafi, N. Ebrahimiadib, R. Roohipourmoallai, A. D. Farahani, M. I. Fooladi, and E. Khalili Pour, “Automated diagnosis of plus

- disease in retinopathy of prematurity using quantification of vessels characteristics,” *Scientific Reports*, vol. 14, no. 1, p. 6375, 2024.
- [24] R. Turior, D. Onkaew, B. Uyyanonvara, and P. Chutinantvarodom, “Quantification and classification of retinal vessel tortuosity,” *ScienceAsia*, vol. 39, no. 3, 2013.
- [25] M. Patasius, V. Marozas, A. Lukosevicius, and D. Jegelevicius, “Evaluation of tortuosity of eye blood vessels using the integral of square of derivative of curvature,” in *IFMBE Proceedings of the 3rd European Medical and Biological Engineering Conference (EMBECC05)*, vol. 11, 2005.
- [26] V. Kashyap, R. Gharleghi, D. D. Li, L. McGrath-Cadell, R. M. Graham, C. Ellis *et al.*, “Accuracy of vascular tortuosity measures using computational modelling,” *Scientific Reports*, vol. 12, no. 1, p. 865, 2022.
- [27] M. V. da Silva, J. Ouellette, B. Lacoste, and C. H. Comin, “An analysis of the influence of transfer learning when measuring the tortuosity of blood vessels,” *Computer Methods and Programs in Biomedicine*, vol. 225, p. 107021, 2022.
- [28] Y. Wang, X. Zheng, C. He, J. Zhang, and S. Huang, “Improved segmentation of infant retinal images and quantitative vascular analysis,” *IEEE Access*, vol. 12, pp. 181 846–181 857, 2024.
- [29] H. F. Wang, D. M. Wang, J. J. Wang, L. J. Wang, J. Lu, P. Qi *et al.*, “Extracranial internal carotid artery tortuosity and body mass index,” *Frontiers in Neurology*, vol. 8, p. 508, 2017.
- [30] S. A. Q. Badawi, M. Takruri, Y. Albadawi, M. A. K. Khattak, A. K. Nileshwar, and E. Mosalam, “Four severity levels for grading the tortuosity of a retinal fundus image,” *Journal of Imaging*, vol. 8, no. 10, 2022.
- [31] P. Zebic Mihic, J. Arambasic, D. Mlinarevic, S. Saric, M. Labor, I. Bosnjak *et al.*, “Coronary tortuosity index vs. angle measurement method for the quantification of the tortuosity of coronary arteries in non-obstructive coronary disease,” *Diagnostics (Basel)*, vol. 14, no. 1, 2023.
- [32] V. Krivosic, P. Goupillou, F. Buffon-Porcher, H. Morel, S. Guey, R. Tadayoni *et al.*, “Assessment of retinal arteriolar tortuosity in patients with col4a1 or col4a2 mutations,” *Retina*, vol. 45, no. 2, pp. 296–302, 2025.
- [33] Y.-P. Huang, S. Vadloori, E. Y.-C. Kang, Y. Fukushima, R. Takahashi, and W.-C. Wu, “Computer-aided detection of retinopathy of prematurity severity assessment via vessel tortuosity measurement in preterm infants’ fundus images,” *Eye*, vol. 38, no. 17, pp. 3309–3317, 2024.
- [34] Z. H. Zhang, X. Yu, Y. Fu, X. Chen, W. Yang, and Q. Dai, “Meibomian gland density: An effective evaluation index of meibomian gland dysfunction based on deep learning and transfer learning,” *Journal of Clinical Medicine*, vol. 11, no. 9, p. 2396, 2022.
- [35] E. Yeu and C. Koetting, “Meibomian gland structure and function in patients with demodex blepharitis,” *Journal of Cataract and Refractive Surgery*, vol. 51, no. 5, pp. 359–365, 2025.
- [36] Y. J. Wang, M. Ke, and X. M. Chen, “Prospective study of the diagnostic accuracy of the in vivo laser scanning confocal microscopy for ocular demodicosis,” *American Journal of Ophthalmology*, vol. 203, pp. 46–52, 2019.
- [37] X. Yu, Y. Fu, H. Lian, D. Wang, Z. Zhang, and Q. Dai, “Uneven meibomian gland dropout in patients with meibomian gland dysfunction and demodex infestation,” *Journal of Clinical Medicine*, vol. 11, no. 17, 2022.
- [38] N. Cinti, P. J. McKeegan, P. J. Bazira, A. Smith, P. Maliakal, M. Danciu *et al.*, “Differences in internal carotid artery tortuosity in ruptured and unruptured anterior circulation aneurysms. a matched case-control study,” *Neurochirurgie*, vol. 71, no. 1, p. 101613, 2025.
- [39] V. Srinivasan, C. Eswaran, and N. Sriraam, “Approximate entropy-based epileptic eeg detection using artificial neural networks,” *IEEE Transactions on Information Technology in Biomedicine*, vol. 11, no. 3, pp. 288–295, 2007.
- [40] L. Ramos, J. Novo, J. Rouco, S. Romeo, M. D. Alvarez, and M. Ortega, “Computational assessment of the retinal vascular tortuosity integrating domain-related information,” *Scientific Reports*, vol. 9, no. 1, p. 19940, 2019.
- [41] C.-B. Li and Y.-L. Ye, “A comparison of topological entropies for nonautonomous dynamical systems,” *Journal of Mathematical Analysis and Applications*, vol. 517, no. 2, 2023.
- [42] S. K. Kattumannil, E. P. Sreedevi, and N. Balakrishnan, “A generalized measure of cumulative residual entropy,” *Entropy*, vol. 24, no. 4, 2022.